Earth's Future

RESEARCH ARTICLE
10.1029/2021EF002165

Global Cooling Hiatus Driven by an AMOC Overshoot in a Carbon Dioxide Removal Scenario

Soon-Il An[1,2], Jongsoo Shin[1], Sang-Wook Yeh[3], Seok-Woo Son[4], Jong-Seong Kug[2,5], Seung-Ki Min[2,5], and Hyo-Jeong Kim[1]

[1]Department of Atmospheric Sciences/Irreversible Climate Change Research Center, Yonsei University, Seoul, South Korea, [2]Division of Environmental Science and Engineering, Pohang University of Science and Technology (POSTECH), Pohang, South Korea, [3]Hanyang University, ERICA, Ansan, South Korea, [4]School of Earth and Environmental Sciences, Seoul National University, Seoul, South Korea, [5]Institute for Convergence Research and Education in Advanced Technology, Yonsei University, Seoul, South Korea

Key Points:

- In CO_2 removal experiment, change of global mean surface temperature was halted for 40 years during the early net-zero CO_2 emission period
- Cooling hiatus was driven by an excessive heat advection by a delayed and surpassed Atlantic Meridional Overturning Circulation (AMOC) to CO_2 forcing
- AMOC overshoot is due to the salt advection feedback, amplified by enhanced salinity gradient and reduced oceanic stratification

Supporting Information:

Supporting Information may be found in the online version of this article.

Correspondence to:

S.-I. An,
sian@yonsei.ac.kr

Citation:

An, S.-I., Shin, J., Yeh, S.-W., Son, S.-W., Kug, J.-S., Min, S.-K., & Kim, H.-J. (2021). Global cooling hiatus driven by an AMOC overshoot in a carbon dioxide removal scenario. *Earth's Future*, *9*, e2021EF002165. https://doi.org/10.1029/2021EF002165

Received 23 APR 2021
Accepted 25 JUN 2021

Abstract

The reversibility of global mean surface temperature was examined by a transient CO_2 reversibility experiment using an Earth system model. The results showed that after CO_2 ramp-up toward CO_2 quadrupling and ramp-down returned to the present-day level, the global mean surface temperature kept decreasing but stopped to change for ~40 years in the early net-zero CO_2 emission period. This period, referred to a cooling hiatus, resulted from a compensation between Southern Hemisphere cooling and Northern Hemisphere warming. The Northern Hemisphere warming was centered over the North Atlantic. This localized warming was caused by an excessive heat advection by a delayed and surpassed Atlantic Meridional Overturning Circulation (AMOC) to CO_2 forcing. During the progression of CO_2 change, the meridional salinity gradient between subtropic and subpolar regions was enhanced, and the oceanic stratification in subpolar North Atlantic was reduced due to accumulated heat and reduced vertical salt import in the deeper ocean. As AMOC started to recover, consequently, the enhanced salt advection feedback and the relaxed buoyant force resulted in AMOC overshoot.

Plain Language Summary

Whether Earth's climate will be recovered after accomplishing a target goal of Paris Agreement is questionable. Here, we performed an Earth system model simulation to explore the reversibility of earth climate, in which a CO_2 concentration level gradually increases to four times CO_2 of the present-day level and then returns to the present-day level. The CO_2 change leads to change in global mean surface temperature (GMST). However, even after the complete return to the present-day CO_2 level, GMST remained as about 1° higher than the present-day. Furthermore, the cooling trend of GMST halts for about 40 years from a net-zero emmission of CO_2. This cooling hiatus is driven by a compensation between the Northern Hemisphere warming and Southern Hemisphere cooling. The Northern Hemisphere warming is likely due to an excessive thermal transport by ocean current. This ocean current, as an upper branch of Atlantic Meridional Overturning Circulation (AMOC), overly responds to CO_2 forcing than it would do. Such overshoot of AMOC is likely caused by the stronger salt advection of enhanced salinity difference between subarctic and subtropics and the much easier downward motion of surface dense water under a reduced oceanic vertical density difference in a changing CO_2 environment.

1. Introduction

The preindustrial carbon dioxide (CO_2) concentration level was 280 ppm (parts per million), which has become higher than 400 ppm, recently mostly due to fossil fuel burning (Friedlingstein et al., 2019). Increasing CO_2 in the atmosphere leads to global warming as a result of the reduced efficiency of terrestrial long-wave cooling. Several ambitious and feasible efforts are now being considered to combat climate change and to adapt to its effects. For example, "The Paris Agreement" targets to limit global warming to lower than 2°C, preferably to 1.5°C, compared to the pre-industrial level. To limit the increase in temperature and/or stabilize climate change, a mitigation goal of net-zero emissions of CO_2 around mid-century needs to be realized (Masson-Delmotte et al., 2018). This objective could be achieved if carbon dioxide emissions are balanced by the absorption of an equivalent amount of carbon. Further reductions of CO_2 concentrations below the current level might be required to go back to the climate optimum condition and/or avoid the

tipping of climate change (van Vuuren et al., 2013). In this regard, the prospective climate state after the stabilization of the CO_2 concentration and associated driving mechanisms are of interest to the scientific community, and have socioeconomic merit. Obviously, the answer on how the climate state will be in the end is directly linked to the reversibility or irreversibility of a climate system. Here, climate irreversibility means that the system cannot be restored to its initial state or can be restored only on a long timescale (Boucher et al., 2012). The climate system is compose of various climate elements, and each climate element must have different reversibility depending on its intrinsic response time scale, for example, spanning from hours-to-weeks of atmosphere to 100–10,000 years of ice sheet (e.g., Ruddiman, 2013), possibility for tipping (Lenton et al., 2008), and the time scale of forcing (e.g., An et al., 2021).

One way to measure the reversibility and/or irreversibility of a climate system is to simulate a climate system model under the following scenarios: overshoot (Huntingford & Lowe, 2007; Nusbaumer & Matsumoto, 2008), peak-and-decline (Schaeffer et al., 2015), CO_2 reversibility (Andrews & Ringer, 2014), ramp-up and -down (Armour et al., 2011; Boucher et al., 2012; Wu et al., 2011), or zero emissions commitment (MacDougall et al., 2020; Matthews & Weaver, 2010). These scenarios are quite similar to each other. For example, one scenario requires that CO_2 atmospheric concentration increases by a certain rate (e.g., 1% per year) from an initial level to a maximum level, which is two, three, or four times the initial level. Subsequently, the CO_2 concentration either decreases after keeping its CO_2 level constant for a certain period or immediately decreases to the initial level without keeping the CO_2 level constant at any time. One may also allow free evolution of atmospheric CO_2 concentration under net-zero emission after increasing of CO_2 concentration to a certain level (MacDougall et al., 2020). States from further model integration with a fixed initial level of CO_2 concentration, that is, recovering with net-zero emission toward the initial climate condition, can be compared with the initial state to measure the irreversibility of a climate system.

Irreversibility of a variety of physical phenomena was examined under a ramp-up and -down scenario. For example, it was demonstrated that both low-level clouds and ocean stratification in the Southern Ocean exhibit hysteresis, implying a possibility of irreversibility (Boucher et al., 2012). It has been also argued that the irreversibility or multiple ice-cover states over the full range of simulated sea ice conditions and an annually ice-free Arctic Ocean hardly existed (Armour et al., 2011). Another study found significant hysteresis behavior in the precipitation response due to previously accumulated heat in the ocean (Wu et al., 2011). The hysteresis behavior of Atlantic Meridional Overturning Circulation (AMOC) in these kinds of experiments is highly interesting (Haskins et al., 2019; Jackson et al., 2014; Sgubin et al., 2015) because AMOC is one of the major tipping elements that can abruptly shift to a qualitatively different state as the climate forcings change (Lenton, 2011; Swingedouw et al., 2020).

Based on multimodel experiments under various types of ramp-up and ramp-down scenarios, it was shown that AMOC became anomalously stronger during the early recovering period keeping a constant CO_2 concentration, referred to as "overshoot" (Jackson et al., 2014; Wu et al., 2011). The study argued that the magnitude of this overshoot was related to the accumulated salinity in the subtropical Atlantic Ocean. The hydrological cycle change during the previous period of high CO_2 levels, partly through hydrological cycle change, and so enhancing a salt advection feedback during the recovering period. A hysteresis-like response of AMOC was also reported by a subsequent study (Sgubin et al., 2015), in which climate models yielded either stronger or weaker AMOC in the recovering phase compared to their initial states.

Asymmetry between the weakening and recovery of AMOC in its hysteresis loop is a dynamic nature of the AMOC system (An et al., 2021; Haskins et al., 2019). Therefore, the asymmetric changes in AMOC are expected under the CO_2 ramp-up and -down scenario. In this study, we investigated the changes in AMOC and its impact on global climate by performing 28 ensemble experiments of CESM 1.2 (Yu & Pritchard, 2019) under CO_2 ramp-up and -down scenario (Methods). The main focus has been given to the following aspects: (a) How does the North Atlantic Ocean respond to the CO_2 ramp-up and -down scenario? (b) What drives the sea surface temperature (SST) change in the subarctic Atlantic Ocean? (c) What are the major processes responsible for changes in SST in subarctic Atlantic? (d) What is the driving mechanism for the excessive response of SST to the changing CO_2 forcing?

2. Methods

2.1. Model Configuration

In this study, we used the Community Earth System Model version 1.2 (CESM1.2) (Hurrell et al., 2013), which is composed of the atmosphere (The Community Atmospheric Model version 5, CAM5), ocean (The Parallel Ocean Program version 2, POP2), sea ice (The Community Ice Code version 4, CICE4), and land models (Community Land Model version 4, CLM4). The atmospheric model had a horizontal resolution of ~1° × 1° and 30 vertical levels (Neale et al., 2012). The ocean model had 60 vertical levels, with a longitudinal resolution of 1° and a latitudinal resolution of 0.3° near the equator that gradually increases to 0.5° near the poles (Smith et al., 2010). The land model comprised the carbon-nitrogen cycle (Lawrence et al., 2011).

2.2. Experimental Design

Two idealized CO_2 pathways were applied (Figure 1a): the constant and varying scenarios. These scenarios were similar to the protocol of the carbon cycle reversibility experiment (CDR-reversibility) except for the initial CO_2 level (Keller et al., 2018). The constant CO_2 scenario was simulated for 900 years with 367 ppm as the present-day CO_2 content, referred to as the present-day period (PD). Subsequently, the varying CO_2 scenario with 28 ensemble members was applied, in which the CO_2 concentration increased 1% per year for 140 years until it quadrupled (i.e., 1,468 ppm; ramp-up period), immediately followed by a symmetric decrease (~1% per year) for 140 years until the CO_2 concentration reached the initial level (367 ppm; ramp-down period). Subsequently, the constant CO_2 (367 ppm) scenario, that is, net-zero emission, was simulated for 220 years (restoring period). The 28 ensemble members were identical except the atmospheric and oceanic initial conditions with different phases of Pacific Decadal Oscillation and Atlantic Multidecadal Oscillation at the PD period. The 28 ensemble members are likely enough to identify a climate signal driven the CO_2 forcing.

2.3. Mixed Layer Temperature and Salinity Equations

The upper-ocean temperature budget was computed as follows (Chemke et al., 2020; Kim et al., 2006):

$$\rho C_p h \frac{\partial [T]}{\partial t} = Q_{\text{net}} - \rho C_p h [\boldsymbol{u} \cdot \nabla_H T] - \rho C_p h [w \cdot \nabla_z T] + \rho C_p h \{[\text{ML mixing}] + \text{subsurface}\}, \quad (1)$$

where the square bracket indicates the depth average within the mixed layer. In Equation 1, T represents the mixed layer temperature and Q_{net} is the net air-sea heat flux (i.e., radiative shortwave [SW] and longwave [LW] fluxes, sensible , latent [LE], and sea ice melting heat flux [MELTH]). Here, the positive fluxes denote the heat transport from the atmosphere to the ocean. However, all results in this study are shown as anomalies, and thus the positive (negative) anomaly in heat flux indicates anomalous warming (cooling) of ocean. ρ is the reference density (1,027 kg m^{-3}), C_p is the specific heat of seawater at a constant pressure (3985 J kg^{-1} K^{-1}), and h is a mixed-layer depth that varies in time. Here, the mixed-layer depth is defined as the shallowest depth where the local, interpolated buoyancy gradient matches the maximum buoyancy gradient between the surface and any discrete depth within that water column (Large et al., 1997). $\boldsymbol{u}$ and w are the horizontal and vertical velocities, respectively. The first three terms on the right-hand side in Equation 1 are net surface heat flux, horizontal temperature advection, and vertical advection, respectively. The "ML mixing" refers to a mixing process in the mixed layer. The subsurface processes represent entrainment across the lateral induction and vertical diffusion. In this study, the last two terms of Equation 1 were calculated as residuals.

The salinity budget analysis was performed using the following simplified equation (Kim et al., 2006; Qu et al., 2011):

$$\frac{\partial [S]}{\partial t} = \frac{Q_A}{h}[S] - [\boldsymbol{u} \cdot \nabla_H S] - [w \cdot \nabla_z S] + [\text{ML mixing}] + \text{subsurface}, \quad (2)$$

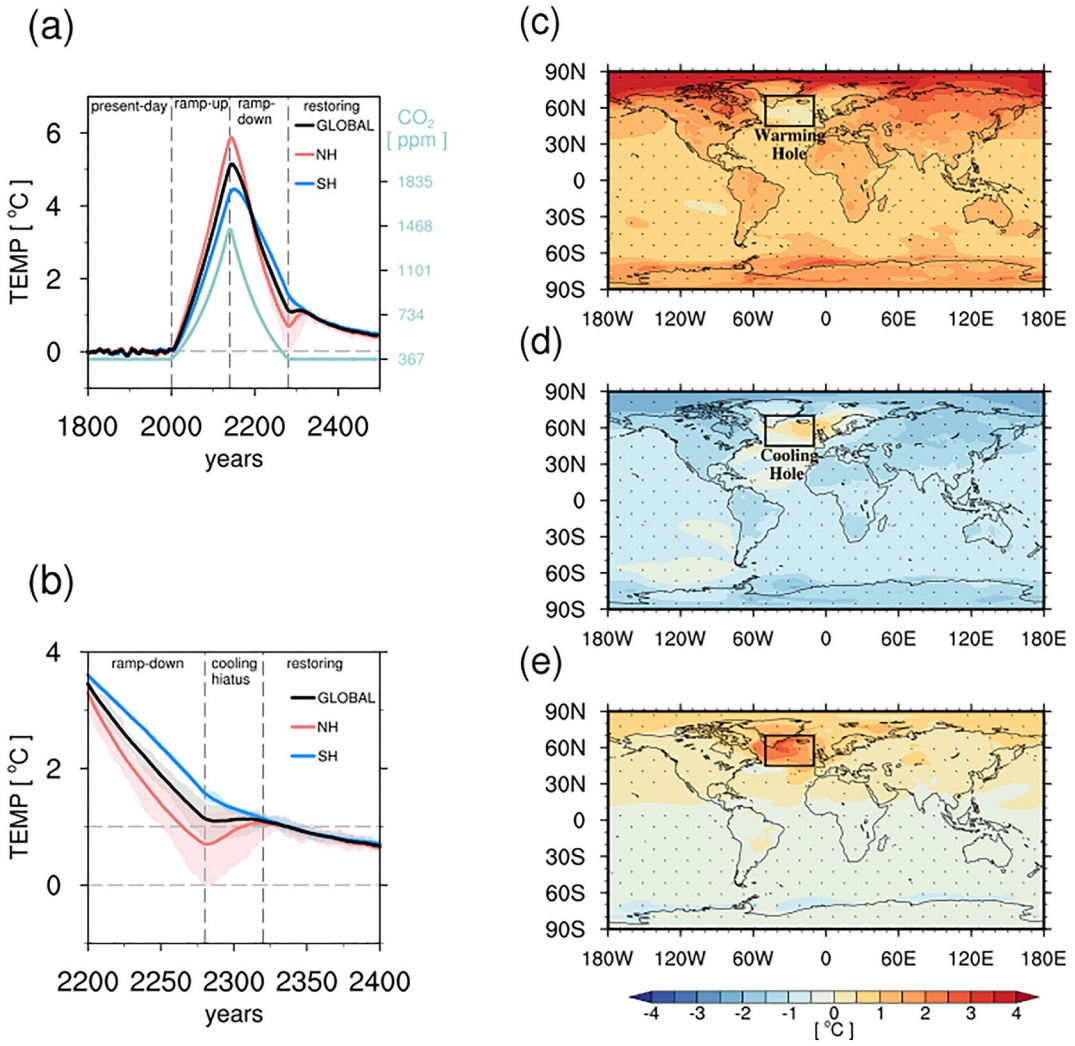

Figure 1. Evolution and changes in global surface air temperature responses to CO_2 forcing. (a) Time series of the 11-year running mean annual surface temperature for the present-day simulation (200 years), the ramp-up and -down period (280 years), and recovery period (220 years). The lines indicate the ensemble mean temperature of Global (black), Northern Hemisphere (NH, red), and Southern Hemisphere (SH, blue) areas, respectively. The shading of each time series indicates ensemble spread. (b) Same as (a) but zoomed into the years 2200–2400 model years. All variables in this figure are deviations from the mean for present-day (PD) period, and mean values of 28 ensemble members. (c) and (d) tendencies of ensemble-mean annual-mean surface temperature at 2°C of GMST change during the ramp-up and -down periods, respectively. Here, tendency is a temperature change. Details are in the text. (e) Same as (c) but for the cooling hiatus period. Units of (c)–(e) are degree celsius. The dots denote the significance of ensemble spreads. The northern subpolar Atlantic Ocean (45°–70°N, 50°–10°W) is marked as a black box.

This equation is the same as Equation 1, however, a mixed-layer salinity S was applied. The coefficient Q_A represents surface salinity flux, which includes evaporation, precipitation, runoff, ice runoff, and ice melting fluxes. The last two terms of Equation 2 are residuals.

3. Results

3.1. Cold Blob, Warm Blob, and Cooling Hiatus

During the CO_2 ramp-up phase, it was found that the global mean surface temperature (GMST) gradually increases up to 5°C compared to the GMST of PD. During the CO_2 ramp-down phase, GMST gradually decreases to ~1.0°C above the PD GMST (Figure 1a). After achieving a constant CO_2 level or net-zero CO_2 emission, the GMST slowly approaches toward the PD level, although it never reaches the exact PD level

(Figures 1a and 1b). Such irreversible or long delays in returning response was also reported in previous studies (Boucher et al., 2012; Chadwick et al., 2013; Ehlert & Zickfeld, 2018), and in particular, the long-delayed response is possibly due to the thermal inertia of the Earth climate system, especially associated with the heat uptake of the ocean. Although the irreversibility of GMST might be temporary, the ensemble mean temperature difference remain significant during the last 200 years of the simulations. The warming episode during the CO_2 ramp-up phase was not homogeneous over the globe, and there were regional differences as shown in the tendency of ensemble-mean annual-mean surface temperature (EMST) at 2°C of GMST that occurred around the year 2067 (Figure 1c). Here, the tendency is defined as difference in EMST between 30-year average (2067–2096) after and 30-year average (2037–2066) before recording 2°C of GMST. The regional features of surface temperature changes were quite similar to the observed trends of temperature change in the 20th century (Figure 2.21 of IPCC AR5 WG1) such as the greatest warming over the Arctic (so-called "Arctic Amplification"), stronger warming over high latitude continents, and weaker warming over the sea, especially in southern tropical oceans. Furthermore, an extremely weak warming tendency was observed over the northern subpolar Atlantic Ocean, similar to the currently observed trend (e.g., Chemke et al., 2020; Keil et al., 2020; Liu et al., 2015). This cold blob or warm hole has been suggested to be driven by the reduced oceanic heat transport associated with a slowing AMOC (Chemke et al., 2020; Kim & An, 2013; Liu et al., 2020; Rahmstorf et al., 2015), the enhanced export of oceanic heat to higher latitudes by subpolar gyre, and cooling by shortwave-cloud feedback (Keil et al., 2020). For example, the freshening over the North Atlantic deep water formation region due to reduced evaporation associated with CO_2 increases disrupts AMOC (Kim & An, 2013), and the increase in low-level clouds due to ocean surface cooling blocks the incoming shortwave radiation (Keil et al., 2020). This cold blob was later replaced by a warm blob during the CO_2 ramp-down phase as shown in the tendency of EMST at 2°C of GMST around the year 2246 (Figure 1d). Again, the tendency is defined as difference in EMST between 30-year average (2246–2275) after and 30-year average (2216–2245) before recording 2°C of GMST. Specifically, this warming trend (warm blob or cooling hole) generally appears over the North Atlantic Ocean, with its maximum extent being located at the northeast direction of the maximum warm hole during the ramp-up period (Figure 1d). This indicates that a similar but opposite physical process as a cold blob might occur for a warm blob as well.

During the early recovery period (2280–2320), the warm blob shown in Figure 1d was further enhanced, especially over the Labrador and Irminger Seas (Figure 1e), indicating that the enhanced heat import into the subpolar gyre region where AMOC is connected. Here, the tendency of EMST during this early recovery period (Figure 1e) is defined as the difference between the average of (2301–2320) and that of (2281–2300). During this period, the global-averaged net radiative flux at the top of atmosphere was negative (Figure S1), indicating that the ocean is likely a heat source (Andrews & Ringer, 2014). Moreover, a moderately warming trend occurs over the Arctic Ocean and North Pacific, and a weakly warming trend widely covers all Northern Hemisphere continents, except at the tropics. The GMST of the Northern Hemisphere also displayed a warming trend between 2280 and 2320, followed by a cooling trend after 2320. The cooling trend was observed over the entire Southern Hemisphere and tropics during the same period (Figure 1e). The strongest cooling was observed over the ocean surrounding Antarctica. The hemispheric contrast in surface temperature results in no change in GMST for ~40 years (2280–2320), that is, a cooling hiatus, through compensation in opposite temperature changes between Northern and Southern hemispheres. In the following section, we mainly focus on this peculiar change in the surface temperature change.

3.2. Surface Heat Budget Over the North Atlantic Subpolar Ocean

To assess the cause of the North Atlantic subpolar ocean (ASPO) temperature change, heat budget analysis of the ocean mixed layer (OML) temperature was conducted over the ASPO (45°–70°N and 50°–10°W; boxed in Figure 1c; Figures 2b–2d). As shown in Figure 2a, the ASPO temperature gradually increased up to ~2°C compared to PD during the ramp-up period, however, the rate of increase was relatively weaker compared to that at other same or higher latitude regions (Figure 1c). During the ramp-down period, ASPO temperature sharply decreased by ~3°C compared to PD, and subsequently started to increase before the CO_2 concentration reached the PD level. During the restoring phase, the ASPO temperature kept increasing and reached its maximum, representing a 2°C warmer climate in 2320, which is almost equal to the temperature at maximum CO_2 concentration. This rapid warming from the 2220s–2320s was much stronger than that in the CO_2 ramp-up warming period (2000–2140), although the CO_2 concentration decreased and later

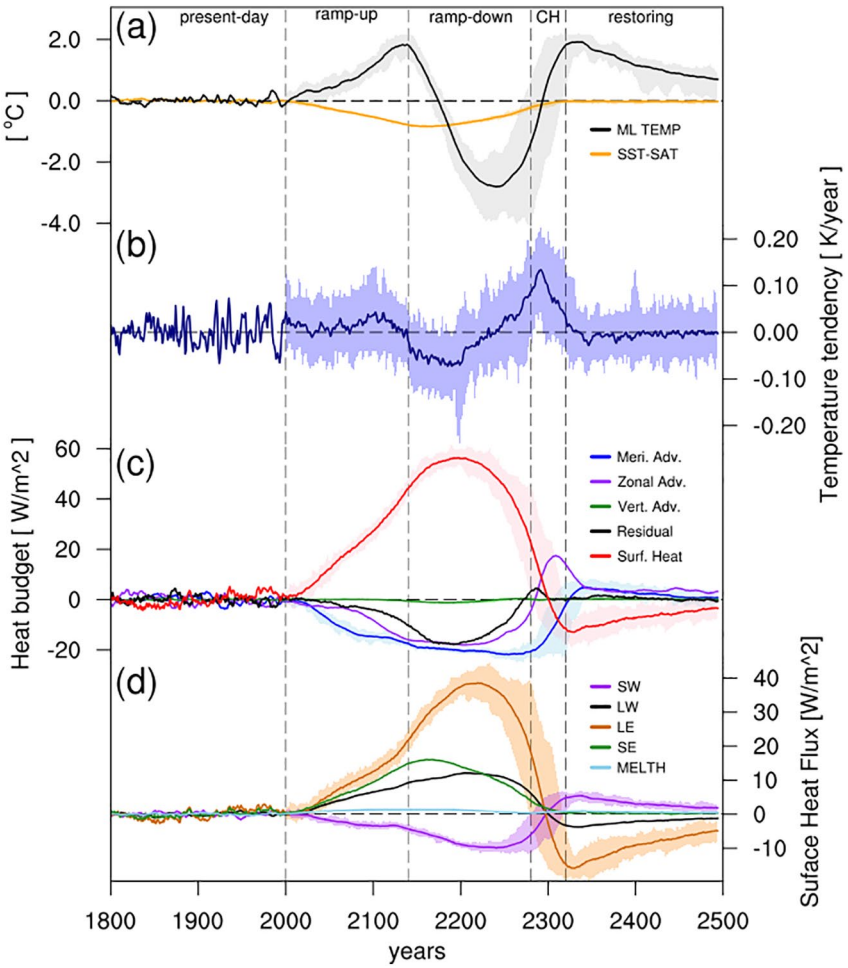

Figure 2. Evolution of mixed layer temperature and heat budget. Time series of the 11-year running mean of (a) annual mixed layer temperature over northern subpolar Atlantic Ocean (ML TEMP, black line) and difference (orange line) between near surface air temperature (SAT) and sea surface temperature (SST), (b) its tendency (K/year), (c) its heat budget (W/m^2), and (d) a corresponding surface heat flux (W/m^2) area-averaged over northern subpolar Atlantic Ocean. The shading of each time series indicates ensemble spread. Meridional heat advection (Meri. Adv., blue; $-\rho C_p h\left[v \cdot \nabla_H T\right]$), zonal heat advection (Zonal Adv., purple; $-\rho C_p h\left[u \cdot \nabla_H T\right]$), vertical heat advection (Vert. Adv., green), residual (black), and surface heat flux (Surf. Heat, red; Q_{net}) are represented. Shortwave (SW), longwave (LW),latent heat flux (LE), sensible (SE), and sea ice melting heat flux (MELTH) indicate net shortwave radiative flux (purple line), net longwave radiative flux (black), latent heat flux (brown), sensible heat flux (green line), and heat flux by melting of sea ice (skyblue), respectively. All values are deviations from their mean for PD period, and solid lines indicate the mean values of 28 ensemble members.

reached a constant level similar to PD. After the peak, the ASPO temperature slowly decreased (Figure 2b) although warmer conditions compared to PD period were maintained for more than 100 years.

The increasing ASPO temperature during the ramp-up phase was mainly due to warming by surface heat flux, whereas cooling by the zonal and meridional oceanic heat advection along with the residual processes partly compensated the warming, causing a weak warming in ASPO (Kim & An, 2013) (Figure 2c). The residual is the sum of all other processes except net surface heat fluxes, and horizontal and vertical advection such as three-dimensional thermal diffusion and thermal advection by subgrid scale eddies. During the ramp-down phase, the surface heat flux kept increasing until the year 2200 despite a decrease in CO_2 concentration because although the evaporative cooling gets reduced as the ocean surface cools (Figures 2a and 2d), cooling by other processes overcompensates this. Therefore, ASPO temperature declined until approximately the year 2240, when its minimum temperature was observed. Subsequently, the zonal heat ad-

vection started to increase, followed by an increase in meridional heat advection. The net surface heat flux decreased as the ocean surface warmed up, and the difference between ocean temperature and surface air temperature decreased (orange line in Figure 2a). The residual also increased during the ramp-down period, and became positive during the recovery period. The negative tendency of ASPO temperature due to the residual was mainly due to vertical diffusion, as oceanic stratification increased during the ramp-down period (see Figure 4f). The recovery toward the positive tendency was related to the reduced oceanic stratification as the AMOC recovered. The positive ASPO temperature during the cooling hiatus period and almost zero tendency in the remaining recovery period resulted in an ASPO temperature peak of 2°C at the end of the cooling hiatus period. The positive ASPO temperature tendency is likely to be a combination of the positive tendency due to surface heat flux and zonal heat advection, and the reduced negative tendency is probably associated with the meridional heat advection. Here, it is important to note that the positive tendency due to surface heat flux was a byproduct (or passive feedback) resulting from horizontal heat advection.

It was found that the net heat flux at the surface mainly follows the latent heat flux (LE), and both sensible heat flux (SE), and net long-wave radiation (LW) contribute to the surface heat flux in a similar way, although their contribution was lower than LE. The net short-wave radiation (SW) exhibited almost a mirror image of LW with a smaller magnitude. Climatologically, the evaporative cooling (LE) occurs over ASPO due to the colder air originating from the continent over the warmer ocean surface, especially during boreal winter. During the ramp-up period, the faster warming of near surface air than the ASPO surface (i.e., decreased temperature difference between atmosphere and ocean in Figure 2a) resulted in the reduction of evaporative cooling (Figure 2d). The reduced air-sea temperature difference was maintained during the ramp-down period because of the faster cooling of ASPO than that of the atmosphere, however, the magnitude of the difference gradually decreased because of the increase in ocean surface temperature until the end of the ramp-down phase (Figure 2a). Furthermore, the ocean mixed layer depth in ASPO reduced from 150 m in PD to 60 m during the ramp-down period, which increased the efficiency of ocean surface temperature and LE change (not shown). LE and SE were determined by the air-sea interaction at the surface. However, they relied more on the change in ocean surface temperature, driven by the oceanic heat advection associated with AMOC and ocean circulation such as subpolar gyre (Keil et al., 2020). Therefore, the warming tendency by surface heat flux (especially LE and SE) is likely associated with a passive feedback due to temperature changes in the upper ASPO by horizontal heat advection.

3.3. Role of Ocean Circulations in Cooling Hiatus

The horizontal oceanic heat transport over ASPO is directly linked to AMOC and subpolar gyre circulation. As shown in Figure 3a, the AMOC decreased during the ramp-up period. It decreased further until the year 2180 in the middle of the ramp-down period, with a recorded strength of ~10 Sv (Sv = 1 million m^3 s^{-1}), which is only half of PD. The strongest cooling tendency occurred at 2200 (Figures 2a and 2b), and thus, the temperature change lagged AMOC by ~20 years (see Figure S2). After the year 2180, AMOC increased quickly up to ~25 Sv until the cooling hiatus period, and subsequently, it decreased slowly. Therefore, the difference between the maximum and minimum AMOC strength was ~15 Sv. AMOC change was almost in-phase with salinity change over ASPO, and was slightly ahead of the density change. Therefore, the local density change, especially due to salinity change over the oceanic convection region within ASPO, is strictly linked to AMOC. In this respect, we can expect that the feedback processes associated with surface hydrology change and oceanic salt advection control AMOC change.

A negative tendency of salinity started to appear right after the CO_2 increase, and its maximum negative tendency was marked at the highest CO_2 concentration (Figure 3b). Around 2200, the tendency changed its sign from negative to positive, which aligned with the minimum salinity over ASPO. The maximum positive salinity occurred during the cooling hiatus period, and the tendency sign changed again at the end of the cooling hiatus. Thus, the maximum salinity was observed at the end of the cooling hiatus. Afterward, the salinity tendency converged to zero. The negative salinity trend during the ramp-up was driven primarily by zonal salinity advection, and secondly by the increasing surface freshwater flux (i.e., mainly by the reduced evaporation, Liu et al., 2020; Ma et al., 2020) and meridional salinity advection (Figures 3c and 3d). During the ramp-down period, the zonal salinity advection started to increase, and thus, the phase change in the zonal salinity advection was similar to that of the total salinity tendency. While the meridional sa-

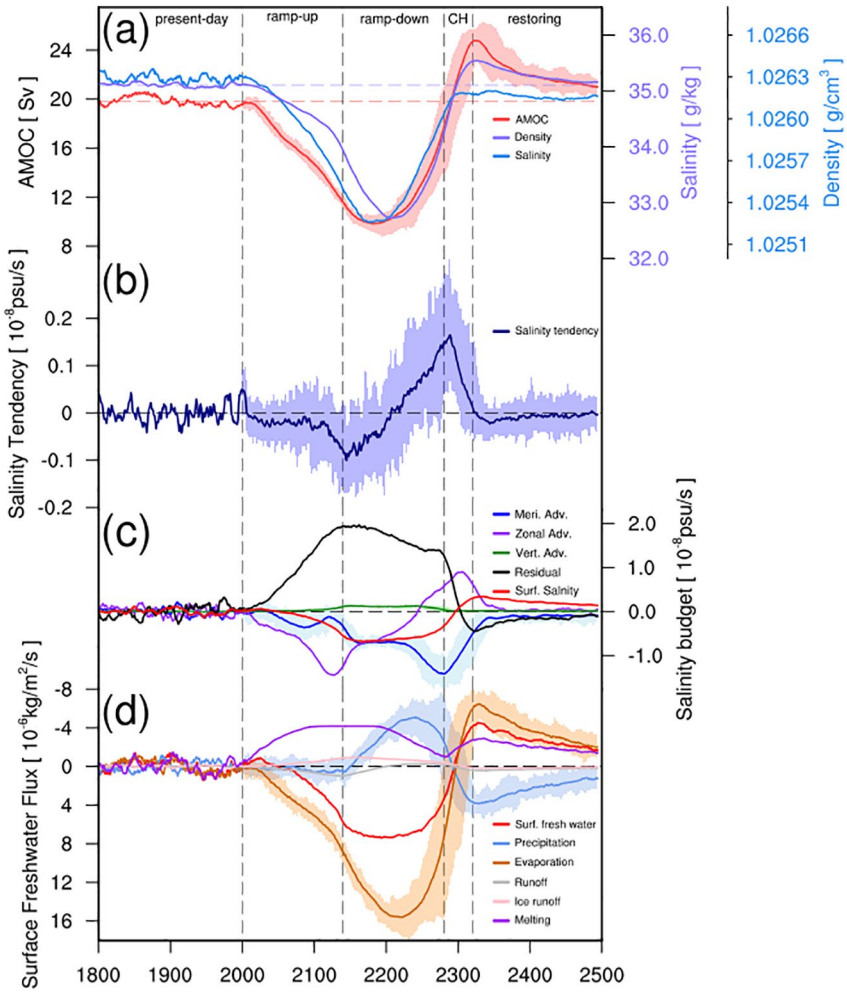

Figure 3. Evolution of Atlantic Meridional Overturning Circulation (AMOC) and mixed layer salinity, density, and salinity budget. (a) Time series of the 11-year running mean of annual-mean AMOC index (maximum value at 26N, red line, Sv), mixed layer salinity (purple line, g/kg), and density (blue line, g/cm^3); (b) salinity tendency (psu/s); (c) salt budget (psu/s); and (d) surface freshwater flux (kg/m^2/s) averaged over northern subpolar Atlantic Ocean. Meridional salt advection (Meri. Adv., blue; $-\left[v \cdot \nabla_H S\right]$), zonal salt advection (Zonal Adv., purple; $-\left[u \cdot \nabla_H S\right]$), vertical salt advection (Vert. Adv., green), residual (black), and surface salinity flux (Surf. Salinity, red; $\left(\frac{Q_A}{h}\right)\left[S\right]$) are represented. Surface freshwater flux (Surf. fresh water, red), precipitation (sky blue), evaporation (brown), runoff (gray), ice runoff (Iceoff, pink), and sea ice melting (Melting, purple) are also represented. All values are deviations from their mean for PD period, and mean values of 28 ensemble members if applicable.

linity advection kept decreasing by the end of the ramp-down phase, the negative salinity tendency was maintained by the reduced evaporation. The residual, which indicates vertical salinity diffusion, produced a substantial positive salinity trend during the ramp-up and -down periods. This is because the enhanced vertical stratification in the upper ocean prevented the diffusion of low salinity water of the subsurface to the surface. Note that vertical salinity advection was very weak. The change in zonal salinity advection was likely related to the change in the subpolar gyre. The surface wind stress curl over ASPO was reduced during the ramp-up phase, thereby suppressing the subpolar gyre circulation. The stress increased during the ramp-down phase, leading to enhanced subpolar gyre circulation (not shown). Therefore, the zonal salinity advection change was associated with the change in surface wind stress. Although the meridional salinity advection did not strictly follow changes in AMOC, it can be suggested that the decreasing trend in salinity induced by meridional salinity advection was related to AMOC. Interestingly the zonal salinity advection changed prior to changes in meridional advection and residual terms. All salinity budget terms changed

10.1029/2021EF002165

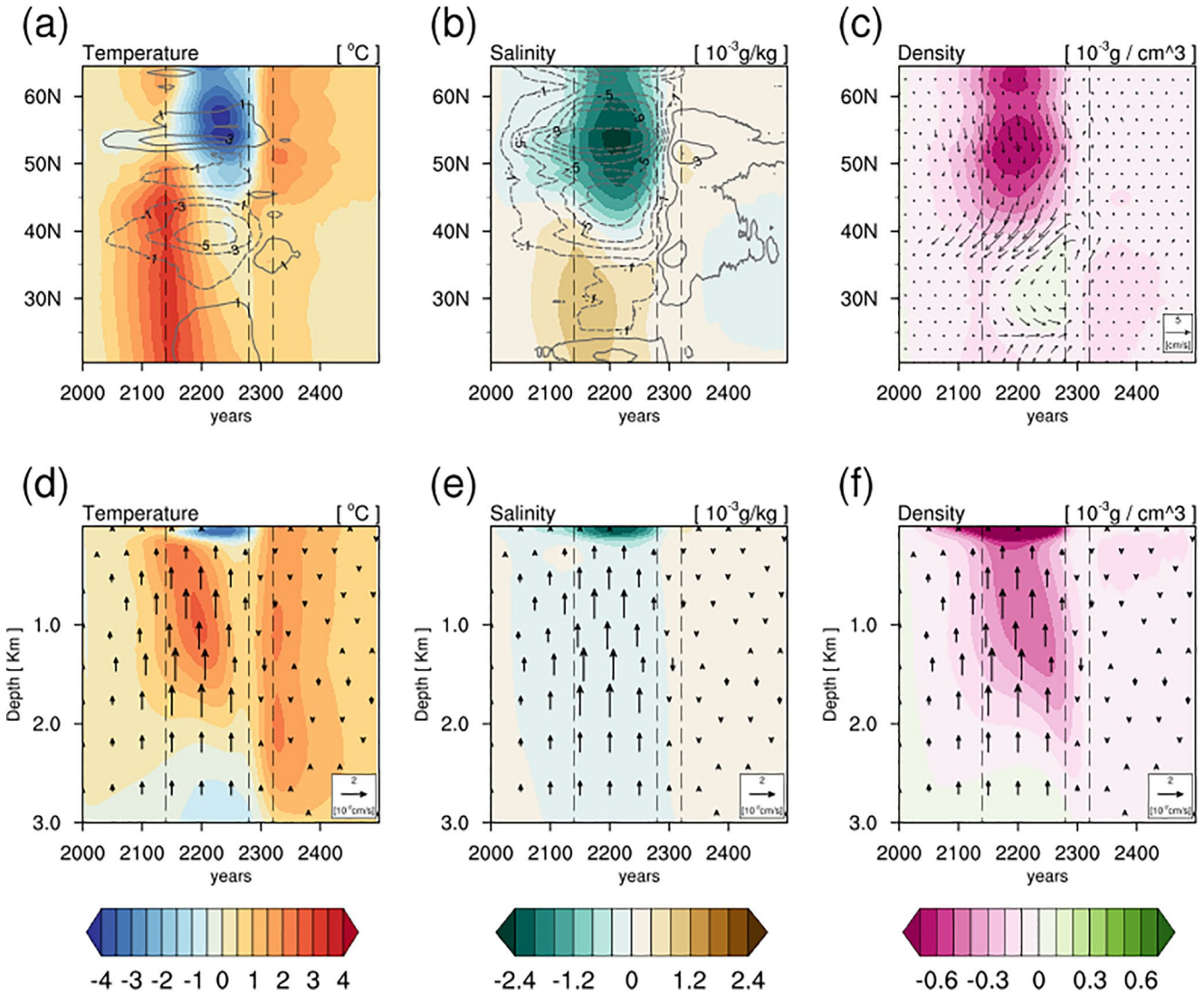

Figure 4. Evolution of potential temperature, salinity, potential density, and currents. Time–latitude section of the 11-year running mean of 100 m depth (a) annual potential temperature with zonal current (contour line), (b) salinity with meridional current (contour line), and (c) potential density with horizontal current (vectors). Zonal mean is taken for the Atlantic Ocean basin (20°–65°N, 80°–0°W). Negative zonal and meridional currents represent dashed lines, and their units are cm/s. Time–depth section of 11-year running mean of ocean (d) annual potential temperature, (e) salinity, and (f) potential density area-averaged over northern subpolar Atlantic Ocean (45°–70°N, 50°–10°W). The vectors represent vertical currents. All values are deviations from their mean for the PD period, and mean values of 28 ensemble members.

their tendency during the hiatus period (Figure 3c), and subsequently, the total salinity tendency changed its sign from positive to negative (Figure 3b). Consequently, the salinity as well as AMOC were maximized at the end of the cooling hiatus period.

Positive freshwater flux, which induced a negative salinity trend was mainly driven by reduced surface evaporation (Figure 3d). The reduced sea ice melting, whose rate increased during the ramp-up phase and decreased during the ramp-down phase, and the reduced precipitation especially during the ramp-down, induced a negative freshwater flux leading to a positive salinity trend (see also Figure S3). As previously mentioned, each of the surface freshwater flux terms changed its tendency during the hiatus period (Figure 3d).

3.4. Overshoot of AMOC

As the AMOC started to recover, anomalously higher salinity in the subtropical region was advected to the subpolar region (Figure 4b) (Haskins et al., 2019; Wu et al., 2011). During the slowing down period of AMOC, the suppressed salt exported from the subtropics (southward current) led to an increase in salinity in the subtropics (Figures 4b and 4c). The increase in subtropical salinity was also driven by the reduced atmospheric freshwater flux (i.e., precipitation minus evaporation; e.g., Figure S3) during the ramp-up to -down period, which is a general response induced by the CO_2 driven global warming (Allen & Ingram, 2002; Christensen et al., 2013). Therefore, as AMOC recovered, the enhanced salt advection feedback associated with stronger meridional salinity gradient and the recovered northward current induced stronger northward salt transport, and then the zonal advection of the salt by subpolar gyre into the region for deep convection promoted the overshoot in AMOC.

The surface warming of the subpolar region during the ramp-up period was slowly diffused to the deeper ocean during the ramp-down period (Figures 4a and 4d), and the lower salty surface water during the ramp-down period was also slowly diffused to the deeper ocean (Figure 4e). Furthermore, as a fresh buoyant cap formed at the ocean mixed layer during the ramp-down period (Figures 4e and 4f), the subsurface and deep ocean water became isolated from the surface fluxes, and thus remained warm (Figure 4d) (Haskins et al., 2019). These effects led to a less stratified density profile and caused instability in the water column, especially around the end of the ramp-down. This could lead to an overshoot in AMOC by promoting convection during the cooling hiatus period (Figure 4f).

4. Conclusions

In this study, the transient CO_2 reversibility experiment, after returning to the initial CO_2 level, showed a pause in the GMST cooling trend for ~40 years, that is, global cooling hiatus. This cooling hiatus was caused by a combination of the oceanic zonal heat advection associated with subpolar gyre (Keil et al., 2020), meridional heat advection by the overshoot of AMOC, and the passive feedback by the latent heat flux. The AMOC overshoot was also simulated by other climate models, and we found that the overshoot intensity of AMOC depends on how much salinity gradient between the North Atlantic deep water formation region and subtropical Atlantic builds up during CO_2 forcing period (Sgubin et al., 2015), as well as how much the oceanic stratification is developed as shown in this study. During the progression of CO_2 change, the salt advection feedback due to the increased meridional salinity gradient between subtropic and subpolar regions was enhanced, and the oceanic stratification due to accumulated heat and reduced vertical salt import in the deeper ocean was reduced. Consequently, as AMOC started to recover, these two effects drove AMOC overshoot.

This study indicates that GMST will not simply decrease after the net CO_2 emission becomes zero. A delayed and excessive oceanic circulation response including AMOC overshoot to CO_2 forcing might lead to a warm environment for several decades in the early mitigation phase including a global hydrological change (Figure S3). Furthermore, the strong climate variability, especially over the Northern Hemisphere, is also expected in this period (see the large ensemble spread in Figure 1b).

One of the main oceanic circulation inside ASPO is the subpolar gyre (SPG), which plays an important role in transporting heat and salt (Moreno-Chamarro et al., 2017), especially into the Labrador Sea, where a core of the downwelling branch for the AMOC is located. For example, the heat and salt transport by Irminger current and the freshwater export from Baffin Bay to Labrador Sea mostly influence the strength of AMOC. However, we did not consider the internal processes of ASPO, while taking the areal average over ASPO. Therefore, the understanding on an interaction between AMOC and SPG will provide a clue on the detailed structure of SST change in North Atlantic Ocean, which will be our next project.

Data Availability Statement

These data are available at https://data.mendeley.com/datasets/f5ry6hgxkw/2.

Acknowledgments
This work was supported by the National Research Foundation of Korea (NRF) grant funded by the Korea government (MSIT) (NRF-2018R1A5A1024958). The CESM simulation was carried out on the supercomputer supported by the National Center for Meteorological Supercomputer of Korea Meteorological Administration (KMA), the National Supercomputing center with supercomputing resources, associated technical support (KSC-2019-CHA-0005), and the Korea Research Environment Open NETwork (KREONET).

References

Allen, M. R., & Ingram, W. J. (2002). Constraints on future changes in climate and the hydrologic cycle. *Nature*, *419*(6903), 228–232. https://doi.org/10.1038/nature01092

Andrews, T., & Ringer, M. A. (2014). Cloud feedbacks, rapid adjustments, and the forcing-response relationship in a transient CO_2 reversibility scenario. *Journal of Climate*, *27*(4), 1799–1818. https://doi.org/10.1175/JCLI-D-13-00421.1

An, S.-I., Kim, H.-J., & Kim, S.-K. (2021). Rate-dependent hysteresis of the Atlantic meridional overturning circulation system and its asymmetric loop. *Geophysical Research Letters*, *48*(1). https://doi.org/10.1029/2020GL090132

Armour, K. C., Eisenman, I., Blanchard-Wrigglesworth, E., McCusker, K. E., & Bitz, C. M. (2011). The reversibility of sea ice loss in a state-of-the-art climate model. *Geophysical Research Letters*, *38*(16). https://doi.org/10.1029/2011GL048739

Boucher, O., Halloran, P. R., Burke, E. J., Doutriaux-Boucher, M., Jones, C. D., Lowe, J., et al. (2012). Reversibility in an Earth System model in response to CO_2 concentration changes. *Environmental Research Letters*, *7*(2), 024013. https://doi.org/10.1088/1748-9326/7/2/024013

Chadwick, R., Wu, P., Good, P., & Andrews, T. (2013). Asymmetries in tropical rainfall and circulation patterns in idealised CO_2 removal experiments. *Climate Dynamics*, *40*(1–2), 295–316. https://doi.org/10.1007/s00382-012-1287-2

Chemke, R., Zanna, L., & Polvani, L. M. (2020). Identifying a human signal in the North Atlantic warming hole. *Nature Communications*, *11*(1), 1–7. https://doi.org/10.1038/s41467-020-15285-x

Christensen, J. H., Kanikicharla, K. K., Aldrian, E., An, S. I., Cavalcanti, I. F. A., de Castro, M., et al. (2013). Climate phenomena and their relevance for future regional climate change. *Climate change 2013 the physical science basis: Working group I contribution to the fifth assessment report of the intergovernmental panel on climate change* (pp. 1217–1308). Cambridge University Press.

Ehlert, D., & Zickfeld, K. (2018). Irreversible ocean thermal expansion under carbon dioxide removal. *Earth System Dynamics*, *9*(1), 197–210. https://doi.org/10.5194/esd-9-197-2018

Friedlingstein, P., Jones, M. W., O'sullivan, M., Andrew, R. M., Hauck, J., Peters, G. P., et al. (2019). Global carbon budget 2019. *Earth System Science Data*, *11*(4), 1783–1838. https://doi.org/10.5194/essd-11-1783-2019

Haskins, R. K., Oliver, K. I. C., Jackson, L. C., Drijfhout, S. S., & Wood, R. A. (2019). Explaining asymmetry between weakening and recovery of the AMOC in a coupled climate model. *Climate Dynamics*, *53*(1–2), 67–79. https://doi.org/10.1007/s00382-018-4570-z

Huntingford, C., & Lowe, J. (2007). "Overshoot" scenarios and climate change. *Science*, *316*(5826). https://doi.org/10.1126/science.316.5826.829b

Hurrell, J. W., Holland, M. M., Gent, P. R., Ghan, S., Kay, J. E., & Kushner, P. J. (2013). The community earth system model: A framework for collaborative research. *Bulletin of the American Meteorological Society*, *94*(9), 1339–1360. https://doi.org/10.1175/BAMS-D-12-00121.1

Jackson, L. C., Schaller, N., Smith, R. S., Palmer, M. D., & Vellinga, M. (2014). Response of the Atlantic meridional overturning circulation to a reversal of greenhouse gas increases. *Climate Dynamics*, *42*(11–12), 3323–3336. https://doi.org/10.1007/s00382-013-1842-5

Keil, P., Mauritsen, T., Jungclaus, J., Hedemann, C., Olonscheck, D., & Ghosh, R. (2020). Multiple drivers of the North Atlantic warming hole. *Nature Climate Change*, *10*(7), 667–671. https://doi.org/10.1038/s41558-020-0819-8

Keller, D. P., Lenton, A., Scott, V., Vaughan, N. E., Bauer, N., Ji, D., et al. (2018). The carbon dioxide removal model intercomparison project (CDRMIP): Rationale and experimental protocol for CMIP6. *Geoscientific Model Development*, *11*(3), 1133–1160. https://doi.org/10.5194/gmd-11-1133-2018

Kim, H., & An, S. I. (2013). On the subarctic North Atlantic cooling due to global warming. *Theoretical and Applied Climatology*, *114*(1–2), 9–19. https://doi.org/10.1007/s00704-012-0805-9

Kim, S.-B., Fukumori, I., & Lee, T. (2006). The closure of the ocean mixed layer temperature budget using level-coordinate model fields. *Journal of Atmospheric and Oceanic Technology*, *23*(6), 840–853. https://doi.org/10.1175/jtech1883.1

Large, W. G., Danabasoglu, G., Doney, S. C., & McWilliams, J. C. (1997). Sensitivity to surface forcing and boundary layer mixing in a global ocean model: Annual-mean climatology. *Journal of Physical Oceanography*, *27*, 2418–2447. https://doi.org/10.1175/1520-0485(1997)027<2418:stsfab>2.0.co;2

Lawrence, D. M., Oleson, K. W., Flanner, M. G., Thornton, P. E., Swenson, S. C., Lawrence, P. J., et al. (2011). Parameterization improvements and functional and structural advances in Version 4 of the community land model. *Journal of Advances in Modeling Earth Systems*, *3*(3), 1–27. https://doi.org/10.1029/2011ms000045

Lenton, T. M. (2011). Early warning of climate tipping points. *Nature Climate Change*, *1*(4), 201–209. https://doi.org/10.1038/nclimate1143

Lenton, T. M., Held, H., Kriegler, E., Hall, J. W., Lucht, W., Rahmstorf, S., & Schellnhuber, H. J. (2008). Tipping elements in the Earth's climate system. *Proceedings of the National Academy of Sciences*, *105*(6), 1786–1793. https://doi.org/10.1073/pnas.0705414105

Liu, W., Fedorov, A. V., Xie, S. P., & Hu, S. (2020). Climate impacts of a weakened Atlantic meridional overturning circulation in a warming climate. *Science Advances*, *6*, eaaz4876. https://doi.org/10.1126/sciadv.aaz4876

Liu, W., Huang, B., Thorne, P. W., Banzon, V. F., Zhang, H. M., Freeman, E., et al. (2015). Extended reconstructed sea surface temperature version 4 (ERSST. v4): Part II. Parametric and structural uncertainty estimations. *Journal of Climate*, *28*, 931–951. https://doi.org/10.1175/jcli-d-14-00007.1

MacDougall, A. H., Frölicher, T. L., Jones, C. D., Rogelj, J., Matthews, H. D., Zickfeld, K., et al. (2020). Is there warming in the pipeline? A multi-model analysis of the zero emissions commitment from CO_2. *Biogeosciences*, *17*(11), 2987–3016. https://doi.org/10.5194/bg-17-2987-2020

Masson-Delmotte, V., Zhai, P., Pörtner, H.-O., Roberts, D., Skea, J., Shukla, P. R., et al. (2018). IPCC, 2018: Summary for policymakers. In *Global Warming of 1.5°C. An IPCC Special Report on the impacts of global warming of 1.5°C above pre-industrial levels and related global greenhouse gas emission pathways, in the context of strengthening the global response to the threat of climate change, sustainable development, and efforts to eradicate poverty* (p. 32). Geneva, Switzerland: World Meteorological Organization.

Matthews, H. D., & Weaver, A. J. (2010). Committed climate warming. *Nature Geoscience*, *3*(3), 142–143. https://doi.org/10.1038/ngeo813

Ma, X., Liu, W., Allen, R. J., Huang, G., & Li, X. (2020). Dependence of regional ocean heat uptake on anthropogenic warming scenarios. *Science Advances*, *6*, eabc0303. https://doi.org/10.1126/sciadv.abc0303

Moreno-Chamarro, E., Zanchettin, D., Lohmann, K., & Jungclaus, J. H. (2017). An abrupt weakening of the subpolar gyre as trigger of Little Ice Age-type episodes. *Climate Dynamics*, *48*(3–4), 727–744. https://doi.org/10.1007/s00382-016-3106-7

Neale, R. B., Chen, C.-C., Gettelman, A., Lauritzen, P. H., Park, S., Williamson, D. L., et al. (2012). *Description of the NCAR community atmosphere model (CAM 5.0). NCAR Tech. Note NCAR/TN-486+ STR* (pp. 1–12). National Center For Atmospheric Research.

Nusbaumer, J., & Matsumoto, K. (2008). Climate and carbon cycle changes under the overshoot scenario. *Global and Planetary Change*, *62*(1–2), 164–172. https://doi.org/10.1016/j.gloplacha.2008.01.002

Qu, T., Gao, S., & Fukumori, I. (2011). What governs the North Atlantic salinity maximum in a global GCM? *Geophysical Research Letters*, *38*(7), 1–6. https://doi.org/10.1029/2011GL046757

Rahmstorf, S., Box, J. E., Feulner, G., Mann, M. E., Robinson, A., Rutherford, S., & Schaffernicht, E. J. (2015). Exceptional twentieth-century slowdown in Atlantic Ocean overturning circulation. *Nature Climate Change*, *5*(5), 475–480. https://doi.org/10.1038/nclimate2554

Ruddiman, W. F. (2013). *Earth's climate: Past and future* (3rd ed., p. 445). New York: W. H. Freeman and Company.

Schaeffer, M., Gohar, L., Kriegler, E., Lowe, J., Riahi, K., & van Vuuren, D. (2015). Mid- and long-term climate projections for fragmented and delayed-action scenarios. *Technological Forecasting and Social Change*, *90*, 257–268. https://doi.org/10.1016/j.techfore.2013.09.013

Sgubin, G., Swingedouw, D., Drijfhout, S., Hagemann, S., & Robertson, E. (2015). Multimodel analysis on the response of the AMOC under an increase of radiative forcing and its symmetrical reversal. *Climate Dynamics*, *45*(5–6), 1429–1450. https://doi.org/10.1007/s00382-014-2391-2

Smith, R., Jones, P., Briegleb, B., Bryan, F., Danabasoglu, G., Dennis, J., et al. (2010). *The parallel ocean program (POP) reference manual ocean component of the community climate system model (CCSM) and community earth system model (CESM). LAUR-01853* (pp. 1–140).

Swingedouw, D., Ifejika Speranza, C., Bartsch, A., Durand, G., Jamet, C., Beaugrand, G., & Conversi, A. (2020). Early warning from space for a few key tipping points in physical, biological, and social-ecological systems. *Surveys in Geophysics*, *41*, 1237–1284. https://doi.org/10.1007/s10712-020-09604-6

van Vuuren, D. P., Deetman, S., van Vliet, J., van den Berg, M., van Ruijven, B. J., & Koelbl, B. (2013). The role of negative CO_2 emissions for reaching 2°C-insights from integrated assessment modelling. *Climatic Change*, *118*(1), 15–27. https://doi.org/10.1007/s10584-012-0680-5

Wu, P., Jackson, L., Pardaens, A., & Schaller, N. (2011). Extended warming of the northern high latitudes due to an overshoot of the Atlantic meridional overturning circulation. *Geophysical Research Letters*, *38*(24), 1–5. https://doi.org/10.1029/2011GL049998

Yu, S., & Pritchard, M. S. (2019). A strong role for the AMOC in partitioning global energy transport and shifting ITCZ position in response to latitudinally discrete solar forcing in CESM1.2. *Journal of Climate*, *32*(8), 2207–2226. https://doi.org/10.1175/JCLI-D-18-0360.1